J. Fluid Mech. (2012), *vol.* 713, *pp.* 159–182.
doi:10.1017/jfm.2012.453

Dynamical separation of spherical bodies in supersonic flow

S. J. Laurence[1]†, N. J. Parziale[2] and R. Deiterding[3]

[1]Institute of Aerodynamics and Flow Technology, Spacecraft Department, German Aerospace Center, Bunsenstraße 10, 37073 Göttingen, Germany

[2]Graduate Aerospace Laboratories, California Institute of Technology, Pasadena, CA 91125, USA

[3]Oak Ridge National Laboratory, PO Box 2008 MS6367, Oak Ridge, TN 37831, USA

(Received 27 January 2012; revised 15 July 2012; accepted 10 September 2012; first published online 26 October 2012)

An experimental and computational investigation of the unsteady separation behaviour of two spheres in Mach-4 flow is carried out. The spherical bodies, initially contiguous, are released with negligible relative velocity and thereafter fly freely according to the aerodynamic forces experienced. In experiments performed in a supersonic Ludwieg tube, nylon spheres are initially suspended in the test section by weak threads which are detached by the arrival of the flow. The subsequent sphere motions and unsteady flow structures are recorded using high-speed (13 kHz) focused shadowgraphy. The qualitative separation behaviour and the final lateral velocity of the smaller sphere are found to vary strongly with both the radius ratio and the initial alignment angle of the two spheres. More disparate radii and initial configurations in which the smaller sphere centre lies downstream of the larger sphere centre each increases the tendency for the smaller sphere to be entrained within the flow region bounded by the bow shock of the larger body, rather than expelled from this region. At a critical angle for a given radius ratio (or a critical radius ratio for a given angle), transition from entrainment to expulsion occurs; at this critical value, the final lateral velocity is close to maximum due to the same 'surfing' effect noted by Laurence & Deiterding (*J. Fluid Mech.*, vol. 676, 2011, pp. 396–431) at hypersonic Mach numbers. A visualization-based tracking algorithm is used to provide quantitative comparisons between the experiments and high-resolution inviscid numerical simulations, with generally favourable agreement.

Key words: aerodynamics, flow–structure interactions, shock waves

1. Introduction

The study of aerodynamic interactions between separating bodies in high-speed flow is of interest in such areas as meteoroid fragmentation, the deorbiting of space debris, and launch-vehicle stage separation. Much of the previous work exploring fundamental aspects of such interactions has been performed in the context of the atmospheric disruption of meteoroids. Passey & Melosh (1980) attempted a systematic analysis of the separation behaviour of discrete fragments, assuming a purely lateral separation

† Email address for correspondence: stuart.laurence@dlr.de

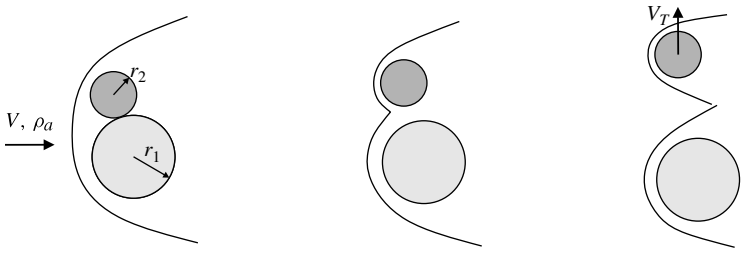

FIGURE 1. The lateral fragment separation model assumed by Passey & Melosh (1980).

between two bodies of radii $r_1 \geqslant r_2$ (see figure 1). Using simple dimensional arguments, they derived the following scaling law for the final lateral separation velocity, V_T, of the smaller body:

$$V_T = \sqrt{C \frac{r_1}{r_2} \frac{\rho_a}{\rho_m}} V. \tag{1.1}$$

Here, V is the velocity of the meteoroid through the atmosphere, ρ_a and ρ_m are the atmospheric and meteoroid densities, respectively, and C is a constant that Passey & Melosh determined through an examination of various terrestrial crater fields to lie between 0.03 and 2.25. Numerical simulations of the symmetrical separation of equally sized bodies were carried out by Artem'eva & Shuvalov (1996) and Artemieva & Shuvalov (2001), yielding values of C in (1.1) of approximately 0.2 and 1 for two and multiple bodies, respectively. These results were incorporated into a model used to simulate specific fragmentation events (Artemieva & Shuvalov 2001).

However, a detailed analysis of a videotaped recording of the Morávka fall (Borovička & Kalenda 2003) revealed serious shortcomings in Artemieva & Shuvalov's model, with measured separation velocities reaching values of up to an order of magnitude larger than those predicted. An explanation for this discrepancy is suggested by the study of Laurence & Deiterding (2011), which demonstrated that findings for equally sized fragments cannot be accurately extended to the separation behaviour of bodies of different sizes. Laurence & Deiterding also showed that the scaling law of Passey & Melosh, (1.1), does not adequately predict the separation behaviour of unequally sized bodies. This is because, contrary to Passey & Melosh's assumption of a purely lateral separation, the smaller body of the two (referred to hereinafter as the secondary body) is subject to a higher axial acceleration and thus travels both laterally and downstream relative to the larger (primary) body. This can lead to a phenomenon referred to as 'shock-wave surfing', in which the secondary body traces a trajectory so as to follow the bow shock of the primary body downstream. In doing so, it develops a significantly larger lateral velocity than would otherwise be possible, since in the surfing configuration, the interacting flow field produces a substantial repulsive lateral force on the secondary body. More specifically, the outer side of this body is exposed to singly shocked flow, whereas the flow on the inner side is processed by the primary bow shock before passing through the secondary shock, and thus experiences a smaller overall stagnation pressure loss related to the weaker entropy rise. Bodies smaller than a critical value do not develop a sufficiently high lateral velocity in the initial stages of separation to commence surfing and are quickly entrained within the flow region bounded by the primary bow shock; bodies significantly larger than the critical value are soon expelled from

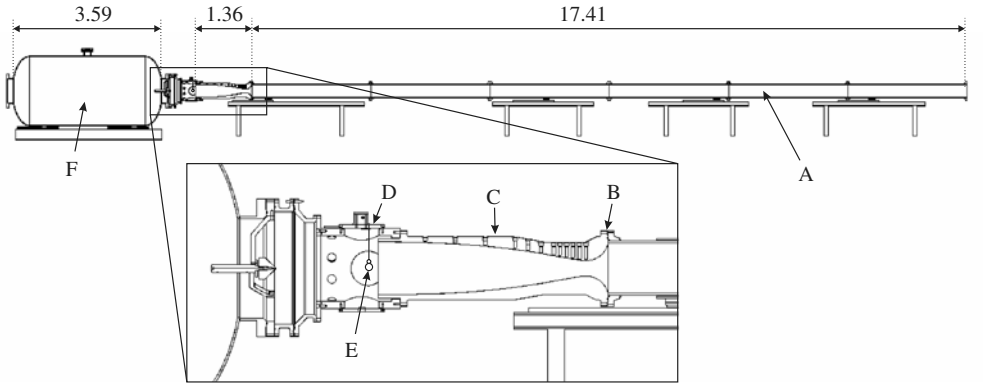

FIGURE 2. Schematic of the GALCIT Ludwieg tube facility (all dimensions are in metres) with a blow-up of the test-section region inset: A, tube (internal diameter 0.298 m); B, diaphragm holder; C, converging–diverging Mach-4 nozzle (exit diameter 0.315 m); D, test section (internal diameter 0.391 m); E, suspended spheres; F, dump tank.

this region. Thus, the ratio of body sizes is a crucial parameter in determining the separation behaviour.

The main intent of the present article is to provide an experimental counterpart and validation to the study of Laurence & Deiterding (2011), which was based on numerical simulations and theoretical analysis alone. The experimental facility employed is the GALCIT Ludwieg tube, capable of producing supersonic flows with Mach numbers of up to 4.0. While this is significantly lower than the hypersonic Mach numbers of the earlier study, a preliminary numerical investigation indicated that the surfing effect still appears at Mach 4. Thus, an extensive experimental investigation was undertaken to explore the separation characteristics of spherical bodies under such flow conditions. The idealized configuration for the study is that of two initially contiguous spheres travelling in supersonic flow, released instantaneously with zero relative velocity and thereafter allowed to fly freely. Spherical geometries are chosen to avoid the additional complication of induced rotations; however, considering that the physical effects described above are in no way particular to flow about spheres, the results obtained are expected to hold, at least qualitatively, for other regular geometries.

The structure of this article is as follows. In § 2, the experimental facility and apparatus are detailed, including a description of the visualization-based tracking technique which constitutes the principal means of measurement. In § 3, the computational model employed alongside the experiments is described and verified. Results of the investigation are presented and discussed in § 4, and conclusions are drawn in § 5.

2. Experimental facility and apparatus

2.1. *Facility*

All experiments were performed in the GALCIT Ludwieg tube, a schematic of which is shown in figure 2. The facility comprises a 17.4 m long tube, an axisymmetric converging–diverging contoured Mach-4 nozzle, a test section and a dump tank. It is a free-jet facility, the cylindrical test section having an internal diameter of 0.391 m compared to the nozzle exit diameter of 0.315 m. The area ratio of the nozzle is

11.96; the difference from the isentropic one-dimensional expansion ratio for a Mach-4 flow (10.72) is due to viscous effects. In the present experiments, the diaphragm was placed between the tube and the nozzle, rather than downstream of the test section. The facility is thus said to be run in 'upstream-diaphragm' mode, with the nozzle, test section and dump tank comprising the downstream section of the facility. In upstream-diaphragm mode, the flow-establishment time is reduced from approximately 25 to 3.5 ms, but the passage of the diaphragm fragments through the test section can be problematic: in a number of the present experiments, fragments were observed in the visualization sequences (described shortly) to strike or influence the free-flying spheres, in which cases the results had to be discarded.

A test begins by inserting a 0.13 mm-thick polycarbonate sheet into the diaphragm holder; the tube and the downstream section are then simultaneously evacuated, typically to 200 Pa. Thereafter, the downstream section is maintained under vacuum while the tube is filled, quickly to 150 kPa, then slowly until the diaphragm ruptures. The mean diaphragm burst pressure in the present experiments was 230 ± 40 kPa.

After diaphragm rupture, an expansion wave propagates upstream into the tube, reflects off the endwall, and propagates downstream. The rupture also generates a shock wave that travels into the downstream section; this is partially reflected from the curved nozzle wall, with the main part of the shock simply propagating into the dump tank. The shock is followed by a contact surface which forms the leading boundary of the main test flow. The partially reflected shock continues to create unsteadiness in the test section for 3–4 ms, whereafter the steady test time commences; steady flow ends upon arrival of the reflected expansion wave. Further details regarding the facility can be found in Mouton & Hornung (2008).

2.2. *Free-stream characterization and measurements*

The free-stream conditions are calculated by considering an unsteady constant-area expansion of the gas in the tube, followed by a steady expansion through the contoured nozzle. First, the Mach number in the tube, M_t, is determined from the area ratio of the tube to the nozzle throat, A_t/A^*, and the ratio of specific heats, γ:

$$\frac{A_t}{A^*} = \frac{1}{M_t}\left(\frac{\gamma+1}{2}\right)^{-(\gamma+1)/(2(\gamma-1))}\left(1+\frac{\gamma-1}{2}M_t^2\right)^{(\gamma+1)/(2(\gamma-1))}. \tag{2.1}$$

The effective reservoir pressure and temperature, p_0 and T_0, are then calculated in ratio to the fill pressure and temperature, p_f and T_f, respectively:

$$\frac{p_0}{p_f} = \left(\frac{1+\dfrac{\gamma-1}{2}M_t^2}{\left(1+\dfrac{\gamma-1}{2}M_t\right)^2}\right)^{\gamma/(\gamma-1)}, \quad \frac{T_0}{T_f} = \frac{1+\dfrac{\gamma-1}{2}M_t^2}{\left(1+\dfrac{\gamma-1}{2}M_t\right)^2}. \tag{2.2}$$

The free-stream conditions (subscript ∞) can then be determined using the steady isentropic one-dimensional relations, assuming a final Mach number of 4.0. Typical conditions for the tests were $\rho_\infty = 0.07$ kg m^{-3}, $p_\infty = 1.4$ kPa and $u_\infty = 670$ m s^{-1}, with a corresponding Reynolds number for a 25.4 mm diameter sphere of 2.7×10^5.

To confirm the accuracy of the derived free-stream conditions, a series of Pitot pressure measurements were performed. A Pitot probe was designed and instrumented with a Kulite XCS-190-10A-L piezoresistive pressure transducer, running through a Dynamics 7600A signal conditioner. An example of a Pitot pressure trace appears in

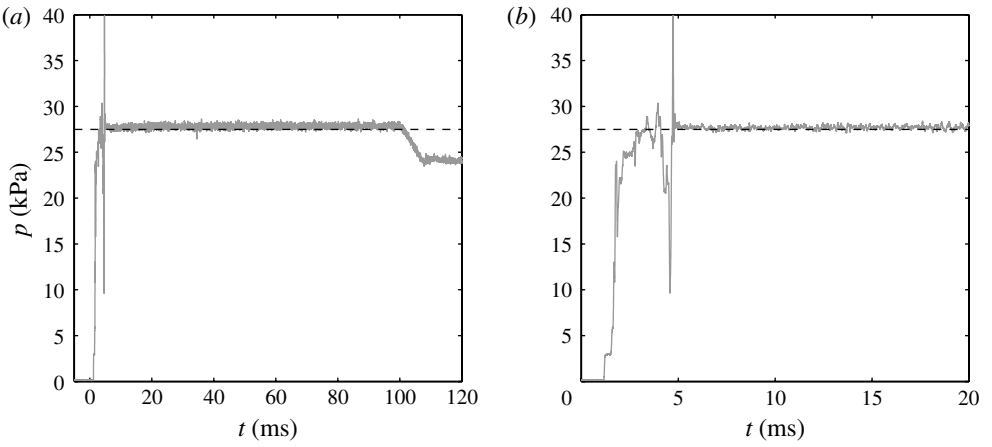

FIGURE 3. A sample Pitot pressure trace of the test-section flow: (*a*) the complete steady flow time of the tunnel; (*b*) the typical test duration employed in the present experiments. The dashed line in both plots indicates the theoretical Pitot pressure derived from the fill conditions.

figure 3: the entire steady flow time of approximately 95 ms is shown in figure 3(*a*), while the test duration of ∼20 ms employed for the present tests is shown in figure 3(*b*). The start-up period of the flow is seen to last approximately 3.5 ms from the instant the initial shock wave produced by the diaphragm rupture reaches the probe. After flow establishment, the standard deviation in the measured Pitot pressure from the mean value over the steady flow period is less than 1 %. In three further Pitot-probe experiments, deviations between 1 % and 2 % were recorded.

Also shown in both plots of figure 3 is a dashed line indicating the theoretical value of the Pitot pressure determined from the free-stream conditions and the Rayleigh–Pitot formula. The theoretical result differs from the mean measured value over the entire steady flow period by 1.2 %, and by 0.7 % between 5 and 20 ms. In the other three Pitot-probe experiments, discrepancies of less than 0.5 % were obtained, indicating that the theoretical estimates of the free-stream quantities give good approximations to the actual experimental values.

2.3. *Model arrangement*

The test articles in this study were spheres manufactured of Nylon 6/6, ranging in diameter from 6.35 to 25.4 mm. Several methods of mounting the spheres in the test section were trialled, the intent being to provide a weak suspension that would be detached and swept away during the flow start-up period while imparting a minimal impulse to the spheres. The most effective solution of those tested was to suspend each sphere by dental floss from the test section roof, with the attachment formed by melting a single fibre from the frayed floss end to the Nylon body; this ensured the weakest part of the suspension was the link between the body and the tether. Two threads in a V-arrangement were attached to the primary sphere, and a single thread to the secondary sphere. Protrusions of less than 100 μm remained on the sphere surfaces after release. A sequence of shadowgraph images showing the start-up of the flow and the detachment of the threads is presented in figure 4. The arrival of the initial shock and the contact surface are visible in the second and third images, respectively. The thread detachment is completed within 1 ms of the initial shock arrival at the spheres.

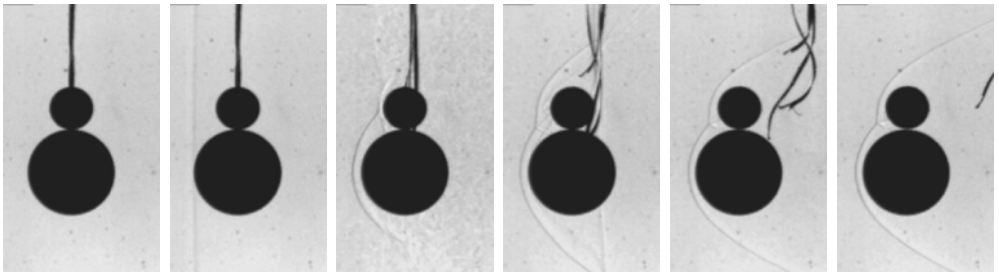

FIGURE 4. Sequence of images showing the start-up of the flow and the detachment of the threads from the spheres, at times (defined from the arrival of the initial shock): −0.08, 0, 0.54, 0.77, 1.00 and 1.23 ms.

2.4. *Visualization set-up and tracking technique*

A 'focused' shadowgraph optical set-up, consisting of a conventional Z-type schlieren arrangement with the knife-edge removed (Settles 2006), was utilized in this study, the intent being to minimize the influence of the visualized flow features on the tracking technique to be described shortly. The focal lengths of the concave mirrors and the focusing lens were 1.5 m and 75 mm, respectively. The light source was a Ostar four-chip 4000 K colour temperature LED mounted onto a surplus air-cooled heat sink, driven continuously by a Harrison Laboratories 6267a DC Power Supply. Images were recorded with a Vision Research Phantom V7.1 SR-CMOS monochrome high-speed camera at a resolution of 512 × 304 pixels; the image magnification was such that a 25.4 mm diameter sphere (as was generally used for the primary body) had an image diameter of approximately 76 pixels. The frame rate and exposure time were 13 kfps and 2–3 μs, respectively.

The sphere displacements, velocities and accelerations during separation were determined through a visualization-based tracking technique. This technique, employed in a basic form in Laurence, Deiterding & Hornung (2007) and subsequently refined in Laurence & Karl (2010) and Laurence (2012), may be summarized as follows. For each image in the recorded sequence, a pixel-resolution Canny edge detection (Canny 1986) is performed (the standard deviation of the Gaussian filter in the edge detection here was 0.8 pixels) and a semi-automated edge-tracing algorithm is used to select the edge points corresponding to each of the sphere outlines. These edge points are then reprocessed using a subpixel-resolution detector, and the sphere centre-of-mass position, (x_0, y_0), and radius, r, in image coordinates are determined by fitting a circle in the least-squares sense to the calculated points. *A priori* knowledge of the physical sphere radii then allows the x_0 and y_0 curves to be converted into physical displacements. Velocities and accelerations can be obtained by numerically differentiating the displacement curves; the resulting amplification of measurement noise, however, usually means that some form of smoothing is subsequently required, especially for accelerations. Alternatively, if either the velocity or the acceleration is assumed to be constant over a certain time period, polynomials of first or second order can be fitted to the displacement profiles to yield mean quantities. The reader is referred to Laurence & Karl (2010) and Laurence (2012) for further details of the technique. In the experimental results presented in § 4, time-resolved velocities are derived from the displacement profiles by second-order central differencing, followed by smoothing with a 5-point moving-average filter. The accelerations (from which the force coefficients are derived) are obtained from a second-order central-difference

approximation to the second derivative of the displacement data, followed by three consecutive applications of a moving-average filter of widths 15, 9 and 7 points, respectively.

In the present application, an additional improvement to the tracking technique was the introduction of a correction for optical distortions, described in the Appendix. To estimate the technique precision, for each experiment a quadratic polynomial was fitted to the displacement of the primary sphere over the time period that it was outside the domain of influence of the secondary sphere, and thus subject to a constant acceleration. We assume that the precision corresponds to the standard deviation of the residuals to this quadratic fit. For a 25.4 mm diameter sphere, a typical value of 2–3 μm was found (corresponding to 0.006–0.01 pixels); this number can be expected to rise to around 6 μm for a 6.35 mm diameter sphere. Although a higher accuracy of ~1 μm was obtained for sphere measurements under calibrated conditions by Laurence (2012), the present estimate is consistent with both the smaller image-sphere diameter and the more challenging experimental conditions.

2.5. *Analysis of experimental errors*

In this subsection we attempt to characterize both the uncertainties in the experimentally measured quantities and the deviations of the experiments themselves from the model problem of the study, i.e. that of two initially contiguous spheres released instantaneously and with zero relative velocity in a steady flow. The quantity of principal interest here is the non-dimensional lateral velocity, $v_y' = \sqrt{\rho_m/\rho_a}v_y/V$; thus, we wish to determine the uncertainties in the quantities in this non-dimensional term, as well as those in the independent parameters that are varied in the investigation, namely the radius ratio, r_2/r_1, and the initial alignment angle between the sphere centres, θ_0.

The diameter and mass of both spheres were measured before each experiment; the precision of the Vernier caliper used for the diameter measurement was 12.7 μm. Over all measured spheres, the maximum deviation recorded in the diameter from its nominal value was 25 μm, giving a maximum discrepancy in the radius ratio ranging from 0.14 % for $r_2/r_1 = 1$ to 0.6 % for $r_2/r_1 = 0.25$. The measured diameters and masses were used to determine the average sphere density, ρ_m; this average value, rather than individually measured values, was used in determining each v_y'. Over all spheres, a mean value of 1.122×10^3 kg m^{-3} with a standard deviation of 0.4 % was obtained. The uncertainty in ρ_m (i.e. the 95 % confidence value) is thus estimated as 0.8 %.

As we have seen in § 2.2, the discrepancy between the measured and theoretically estimated free-stream Pitot pressures and the variation in the measured Pitot pressure during the test time were typically less than 1 % and 2 %, respectively; 95 % confidence intervals for these quantities (the former using the *t*-distribution to account for the small sample size) are estimated as 1.6 % and 3 %. Since the Pitot pressure scales as approximately $\rho_a V^2$, the corresponding errors in v_y' from these free-stream uncertainties will be half the values just quoted. These estimates are also consistent with measurements of the drag coefficients of the primary spheres during the constant-acceleration periods of their trajectories (the same periods used in the precision estimates described in the last paragraph of the previous subsection), in which a standard deviation of 1.1 % was found.

From the displacement-measurement precision estimated in the previous subsection, the precision in v_y (95 % confidence) varies from approximately 0.03 m s^{-1} for 25.4 mm diameter spheres to 0.06 m s^{-1} for 6.35 mm diameter spheres; corresponding

values for the non-dimensional velocity, v_y', are 0.006 and 0.012, respectively. In the Appendix, it is shown that distortions in the optical set-up can lead to systematic errors in v_y of over 1.5 %, but with the applied distortion correction, this error is estimated to be less than 0.5 %. The alignment of the grid used for the correction was checked against the nozzle exit line, and a misalignment of less than 0.02° in the x–y plane was found; any resulting errors can be considered negligible. Additionally, imprecise initial alignment of the spheres in the spanwise direction (i.e. parallel to the light path) will influence the measured lateral velocity; however, the estimated precision of the alignment is of the order of 1°, and even a misalignment of 5° would lead to an error in v_y of less than 0.4 %.

Combining the uncertainties in ρ_m, $\sqrt{\rho_a}V$, and v_y in the manner described in Moffat (1982), we obtain overall uncertainties in v_y' that depend on the values of both r_2/r_1 and v_y' itself: for $v_y' = 0.2$, the 95 % confidence values for $r_2/r_1 = 0.25$, 0.5 and 1.0 are 6.3 %, 4.6 % and 3.5 %, respectively; for $v_y' = 1.0$, these values are 2.1 %, 1.9 % and 1.8 %. At the lower velocity, the uncertainty in v_y tends to be the dominant contribution, whereas at the higher velocity the uncertainty in $\sqrt{\rho_a}V$ dominates.

In addition to uncertainty in v_y', errors in the effective initial conditions, resulting from both the start-up period of the facility and the non-instantaneous detachment of the supporting threads, will also be significant. To determine the impulse imparted by the detaching threads, experiments were performed with a single sphere. The lateral impulse imparted by the single thread suspension was estimated from the measured velocity profiles as approximately 0.12×10^{-4} N s; the axial impulse could not be separated from the flow-induced loading, but the thread angle during detachment suggested that this was negligible. For sphere diameters of 25.4, 12.7 and 6.35 mm, this lateral impulse will give rise to velocities of 0.013, 0.1 and 0.6 m s^{-1}, respectively; the corresponding non-dimensional velocities are 0.003, 0.02 and 0.12. The V-arrangement suspension, as employed for the primary sphere, was found to impart a somewhat larger impulse: for a 25.4 mm sphere, the resulting lateral velocity was typically 0.1 m s^{-1}. Thus, the assumption of a negligible initial relative velocity was best satisfied for $r_2/r_1 = 0.5$; for $r_2/r_1 > 0.5$ the spheres effectively possessed a small negative initial relative velocity (i.e. towards one another) and vice versa.

The influence of the flow start-up period on the effective initial conditions was estimated in the following manner. At the end of the start-up period, the spheres will lie in a particular relative configuration and will be carrying certain velocities. Assuming this combination to be given and that both spheres were initially stationary, the effective initial positions of the spheres will depend on the individual acceleration histories. In particular, the initial positions for idealized step-function accelerations (as assumed in the model problem of the study and implemented in the accompanying computations) will differ from those for the actual experimental accelerations. We can quantify this difference if we assume that the force coefficients (based on the instantaneous flow conditions) are approximately constant during the start-up period and are proportional to the measured Pitot pressure. These assumptions are supported by the observation that, in figure 4, the flow structures are well-established within 1.0 ms of the arrival of the initial shock (compared to the entire start-up duration of approximately 3.5 ms). Thus, using a typical measured Pitot pressure history together with representative force coefficients, we find that the spheres effectively travel further in reaching the same velocity for the experimental acceleration histories, an effect that is more pronounced for smaller spheres. This is caused by the more gradual onset of the experimental aerodynamic loading and means that, in the idealized model problem approximated by a given experiment, the secondary body has a slightly downstream

and laterally separated initial position relative to its actual physical position. This effective initial lateral separation is quite uniform for different r_2/r_1, at 0.3 mm or $0.02r_1$. However, the effective-alignment-angle discrepancy resulting from the offset in the axial direction varies strongly with r_2/r_1: for $r_2/r_1 = 0.25$, 0.5 0.625, 0.75 and 1, the calculated angles are 4.5°, 1.4°, 0.8°, 0.4° and 0°, respectively.

3. Computational modelling

3.1. *Numerical approach*

As in Laurence & Deiterding (2011), we employ the Cartesian fluid solver framework AMROC (Deiterding 2005*b*; Deiterding *et al.* 2005, 2007; Deiterding 2009, 2011*a*,*b*; Ziegler *et al.* 2011) to simulate numerically the fluid–structure interaction of the free-flying spherical bodies. The equations solved to model the inviscid compressible fluid are the Euler equations in conservation-law form

$$\left.\begin{aligned} &\partial_t \rho + \nabla \cdot (\rho \boldsymbol{u}) = 0, \quad \partial_t (\rho \boldsymbol{u}) + \nabla \cdot (\rho \boldsymbol{u} \otimes \boldsymbol{u}) + \nabla p = 0, \\ &\partial_t (\rho E) + \nabla \cdot ((\rho E + p)\boldsymbol{u}) = 0. \end{aligned}\right\} \tag{3.1}$$

Here, ρ is the fluid density, $\boldsymbol{u}$ the velocity vector, and E the specific total energy. The hydrostatic pressure p is given by the polytropic gas equation, $p = (\gamma - 1)(\rho E - (\rho \boldsymbol{u}^{\mathrm{T}}\boldsymbol{u}/2))$. We approximate (3.1) in three space dimensions using a discretely conservative Cartesian finite-volume discretization built on dimensional splitting. The flux-vector splitting approach by Van Leer is used to evaluate an upwinded numerical flux at cell interfaces; the MUSCL-Hancock reconstruction technique with Minmod-limiter is employed to construct a high-resolution method that is of second-order approximation accuracy away from shocks and contact discontinuities, cf. Deiterding (2003).

The spherical bodies are represented on the Cartesian mesh with a scalar level-set function, φ, that stores the signed distance to the nearest point on either sphere surface to each finite-volume cell centre. For non-overlapping spheres, the evaluation of φ is straightforward and we adopt the convention $\varphi > 0$ in the fluid domain and $\varphi < 0$ inside the solid bodies. By utilizing the sign of φ, the first layer of cells inside each body can be identified; the vector of state in these cells is then adjusted to model the relevant non-Cartesian boundary conditions, i.e. a rigid sphere moving with velocity $\boldsymbol{v}$, before applying the unaltered Cartesian finite-volume discretization. The last step involves the interpolation and mirroring of ρ, $\boldsymbol{u}$, and p across the sphere boundary and the modification of the normal velocity in the immersed boundary cells to $(2\boldsymbol{v} \cdot \boldsymbol{n} - \boldsymbol{u} \cdot \boldsymbol{n})\boldsymbol{n}$, with $\boldsymbol{n} = \nabla\varphi/|\nabla\varphi|$, cf. Deiterding (2009). The benefit of this immersed-boundary, aka 'ghost fluid' method (Fedkiw *et al.* 1999) is the natural incorporation of moving bodies. However, the approach usually reduces the approximation accuracy along the immersed boundary, in the present implementation to first order. We mitigate this error by applying automatic, dynamic mesh adaptation along $\varphi = 0$ and additionally to important flow features, specifically to gradients larger than a certain threshold in the fluid density. A representative snapshot of part of the evolving adaptive mesh from one simulation is visualized in figure 5. The adopted mesh adaptation method is the recursive block-structured algorithm for explicit finite-volume discretizations after Berger & Colella (1988), allowing simultaneous adaptive mesh refinement (AMR) in time and space by the same factor, l_j, for each additional level j. In AMROC, the AMR method is fully parallelized for distributed memory

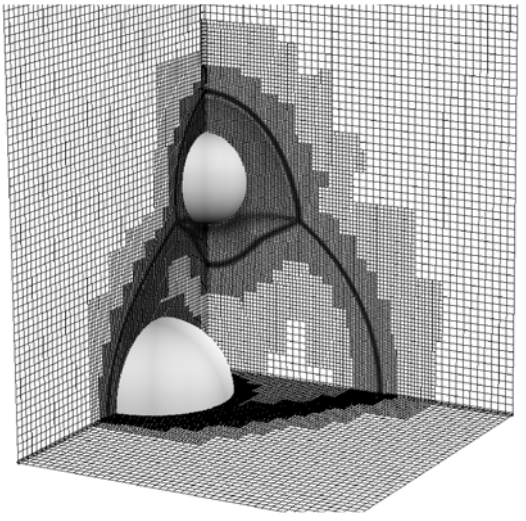

FIGURE 5. Cuts through part of the computational domain of set-up 5 described in table 1 at $t = T + 6.4151$, visualizing the mesh adaptation around the two bodies together with the shock waves on the cut planes. Two additional levels of refinement with $l_{1,2} = 2$ are used.

machines, including automatic load balancing and parallel re-partitioning as the mesh refinement hierarchy changes throughout a computation (Deiterding 2005*a*).

In the simulations described hereinafter, the spheres are always fully enveloped by cells at the highest level of mesh adaptation, and no exchange of kinetic energy by direct contact is allowed to take place. The hydrodynamic force, $\boldsymbol{f}$, on each body is updated after every highest-level time step by integrating the pressure over the body surface, for the purpose of which spherical longitude–latitude grids are temporarily constructed. The position of each sphere's centre, $\boldsymbol{x}$, is then updated by advancing the equation of motion, $\ddot{\boldsymbol{x}} = \boldsymbol{f}/m$, with mass $m = (4/3)\pi r^3 \rho_m$. Finally, the level-set function is re-calculated taking into account both spherical bodies.

3.2. *Model verification*

In order to demonstrate the accuracy and computational performance of the numerical model, in this subsection we discuss in detail a series of consecutively refined computations for a specific case, corresponding to the experiment visualized in figure 9(*c*). Since it is the non-dimensional results that are ultimately of interest, some freedom exists in setting up the problem. In order to provide a benchmark case, we describe the actual configuration simulated.

We study the problem at hand in a Galilean frame of reference and use a computational domain of size $[0, 3] \times [0, 2.5] \times [0.1, 1.9]$. The spheres have radii $r_1 = 0.2$, $r_2 = 0.125$ and their centres are initially located at $(0.35, 1, 1)$ and $(0.3542, 1.3250, 1)$, respectively. The density of both bodies is set to $\rho_m = 2800$ (note that, provided the sphere velocities remain much smaller than the flow velocity, the non-dimensional results are independent of the value of ρ_m/ρ_a). By specifying $\rho_a = 1.4$, $\gamma = 1.4$, uniform initial conditions $\rho_0 = \rho_a$, $\boldsymbol{u} = 0$, $p_0 = 1$, and inflow conditions with $\rho_i = \rho_a$ and $p_i = 1$, the magnitude of the inflow velocity vector becomes identical to the Mach number. An inflow with $\boldsymbol{V}_i = (4, 0, 0)$ is prescribed at the left domain boundary; outflow boundary conditions are applied at all other

No.	Base grid	l_1	l_2	Δx_{min}	Steps	Time (h)	Cores	CPU (h)
1	$150 \times 125 \times 90$	1	1	0.0200	6 131	7.2	128	918
2	$225 \times 188 \times 135$	1	1	0.0133	9 245	16.8	128	2 151
3	$150 \times 125 \times 90$	2	1	0.0100	12 298	40.4	128	5 176
4	$150 \times 125 \times 90$	3	1	0.0067	18 522	72.4	128	9 271
5	$150 \times 125 \times 90$	2	2	0.0050	24 704	143.8	256	36 808
6	$150 \times 125 \times 90$	2	3	0.0033	37 176	318.3	256	81 474

TABLE 1. Computational parameters of the verification study. Six configurations of successively increasing refinement are investigated.

sides. For $t < 0.25$, the inflow velocity is continuously increased by specifying $\boldsymbol{V}_i(1 - \exp(-t/0.05))$ as the boundary condition; for $t \geqslant 0.25$, a constant value of $\boldsymbol{V}_i$ is used. The computation is separated into two parts: during the interval $t = [0, T]$ the spheres are held stationary and a quasi-steady flow field is established; for $t > T$ the two bodies are allowed to move freely according to the forces experienced. The present computation uses $T = 6$ and a final simulated time of $t_e = T + 16$.

The verification study consists of six simulations with progressively increasing resolution; the relevant computational parameters, including the spatial resolution at the highest level of mesh refinement, Δx_{min}, are provided in table 1. Set-ups 1 and 2 use uniform grids; set-ups 3 and 4 employ one additional level of mesh adaptation with refinement factors of 2 and 3; set-ups 5 and 6 use two additional refinement levels with $l_1 = 2$ and l_2 equal to 2 and 3, respectively. All computations employ automatic time step adjustment based on a CFL (Courant–Friedrichs–Levy) condition number of 0.9. The computations were run on an IBM BG/P machine, using 128 or 256 processor cores. Set-up 1 completed in $\sim$7.2 h wall time ($\sim$918 CPU hours). The largest run, set-up 6, computed continuously for almost 2 weeks, requiring $\sim$81 474 CPU hours. Although this number might appear large, the savings from utilizing mesh adaptation are considerable: a uniform computation with the effective resolution of set-up 6 would be $6^4 = 1296$ times more expensive than set-up 1. Multiplying the set-up-1 CPU time yields 1, 189, 728 h, or a potential saving from using AMR of a factor $\sim$14.6.

In figure 6 are plotted the secondary drag and lift coefficients (C_D and C_L) versus the computational time for the six simulations in the verification study. Significant oscillations are observed in the profiles from the coarser simulations: these are caused by the effective change in the body geometry as it moves through the Cartesian computational grid, since the surface of the body is only resolved to the grid resolution. A general trend for the force coefficients to decrease in magnitude with increasing refinement is observed. This can be attributed to a decrease in the lateral primary bow-shock displacement as the resolution is increased, as noted in the refinement study of Laurence *et al.* (2007). In the present case, this will lead to an effective increase in the lateral displacement of the secondary sphere relative to the primary shock, resulting in a more rapid expulsion and giving rise to the observed trends in the force coefficients. Overall, adequate convergence under grid refinement can be inferred from figure 6. Tabulated results from the verification study can be found in the online supplementary material available at http://dx.doi.org/10.1017/jfm.2012.453.

The standard configuration for the numerical simulations that are compared to experiments in § 4.2 is a two-level computation with $l_{1,2} = 2$, as in set-up 5. Analysis

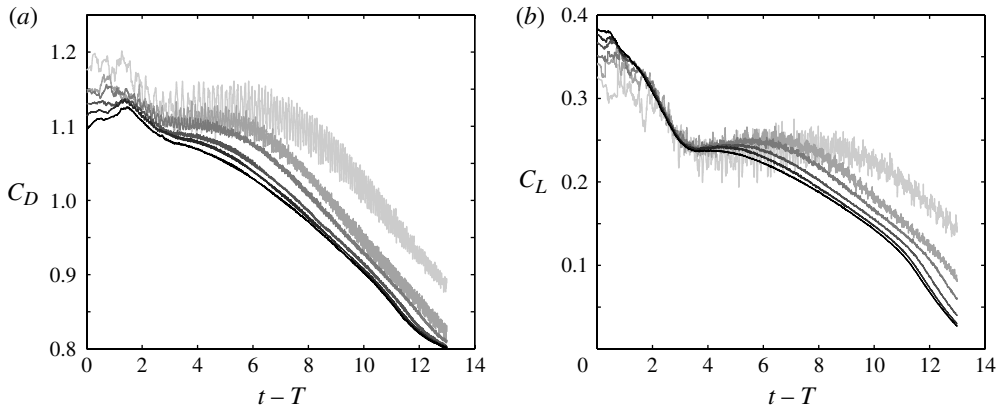

FIGURE 6. Time-resolved secondary force coefficients calculated in the six verification computations described in table 1, with the lightest to darkest curves corresponding to simulations 1 to 6 respectively.

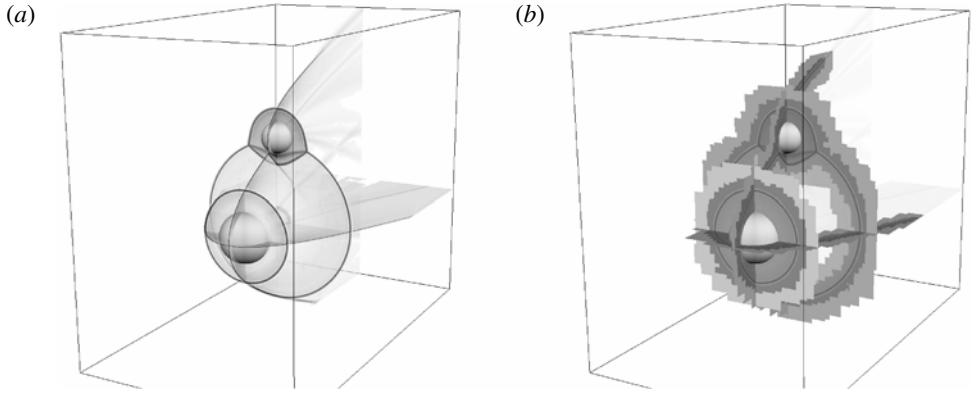

FIGURE 7. Schlieren plots of density (*a*) and domains of the two additional AMR levels (*b*), indicated by different grey scales, for $t = T + 8.974$ in the set-up 5 simulation.

of the grid refinement results suggests that this particular set-up evaluates the lateral velocities of the secondary and primary bodies with deviations of less than 3 % and 2.5 %, respectively, from the fully converged values. Example flow visualizations from simulation 5 are presented in figure 7. Figure 7(*a*) shows planes of pseudo-schlieren (i.e. velocity-gradient magnitude) images perpendicular to the coordinate axes through the sphere centres; figure 7(*b*) visualizes the embedded domains covered by the first and second refinement levels using different grey scales, onto which local pseudo-schlieren visualizations are additionally overlaid. To visualize the dynamics of the separation process, two colour MPG movies corresponding to the images of figure 7 are available at http://dx.doi.org/10.1017/jfm.2012.453. For reference, these movies additionally display the computational time, t, and the x- and y-coordinates of the sphere centres throughout the entire simulation.

As a first validation result, in figure 8 we compare an experimental visualization to a similar image derived from simulation 5. For this single experiment, schlieren

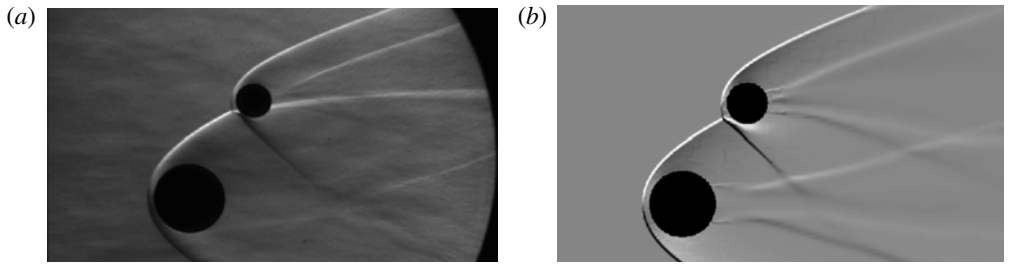

FIGURE 8. Comparison of (*a*) experimentally and (*b*) computationally (set-up 5, $t = T + 7.8367$) derived visualizations of the gradient of the fluid density in the y-direction. In the experimental image, the gradient has been effectively integrated through the fluid domain in the z-direction, while the computational image shows the gradient only on the central plane, $z = 1$.

images were obtained through the introduction of a horizontal knife edge, enabling better visualization of weak features such as the separation regions behind the two spheres. This is intended simply as a qualitative comparison of flow fields, since the configurations are not identical. Moreover, the numerical image visualizes the density gradient in the y-direction only on the central plane, $z = 1$, rather than integrating through the fluid domain; thus, three-dimensional features such as the deflected primary bow shock downstream of the shock–shock interaction are visible in the experimental image but not in the numerical one. The experimental configuration shows earlier flow separation on the rear primary surface, which can be explained by the lack of physical viscosity in the computational model. However, as the aerodynamic forces at this Mach number are dominated by the pressure contribution on the forebody (see, for example, Hoerner 1965), the differing separation points should have only a minor effect on the forces experienced. Aside from this discrepancy, the qualitative flow features show good agreement: in particular, both images clearly show that the flow in the primary wake region does not interact with the bow shock ahead of the secondary body.

4. Results and discussion

4.1. *Qualitative separation behaviour*

The two parameters varied in the experimental investigation were the radius ratio, r_2/r_1, and the initial alignment angle between the sphere centres, θ_0. In figures 9 and 10 are shown sequences of shadowgraph images from experiments in which each of these two parameters was varied independently of the other. First, in figure 9, we see the effect of varying the radius ratio while the sphere centres are kept initially aligned (to within 1°) in the axial direction. Here the convention adopted for the alignment angle is that $\theta_0 = 0$ corresponds to exact axial alignment of the sphere centres, with $\theta_0 < 0$ indicating that the secondary sphere centre initially lies downstream of the primary centre. Systematically increasing r_2/r_1, the behaviour transitions from immediate entrainment of the secondary sphere within the flow region bounded by the primary shock ($r_2/r_1 = 0.25$), to limited surfing followed by entrainment ($r_2/r_1 = 0.5$), extended surfing ($r_2/r_1 = 0.625$), rapid expulsion of the secondary sphere from the region bounded by the primary shock ($r_2/r_1 = 0.75$), and finally symmetrical separation ($r_2/r_1 = 1$). Qualitatively, this is consistent with the behaviour observed at

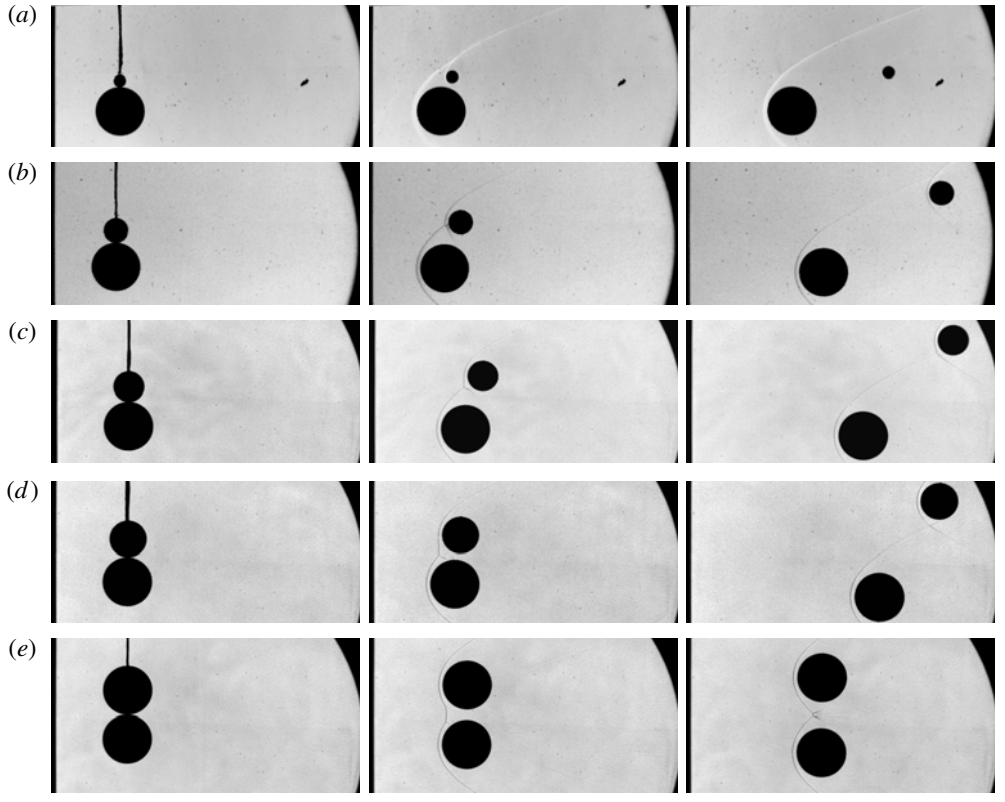

FIGURE 9. Separation behaviour for configurations with various radius ratios and (approximate) initial alignment of the sphere centres in the axial direction. The duration between the first and last image varies between sequences, but is typically around 12 ms: (*a*) $r_2/r_1 = 0.25, \theta_0 = 0.4°$; (*b*) $r_2/r_1 = 0.5, \theta_0 = -0.1°$; (*c*) $r_2/r_1 = 0.625, \theta_0 = -0.7°$; (*d*) $r_2/r_1 = 0.75, \theta_0 = -1.1°$; and (*e*) $r_2/r_1 = 1.00, \theta_0 = -0.6°$.

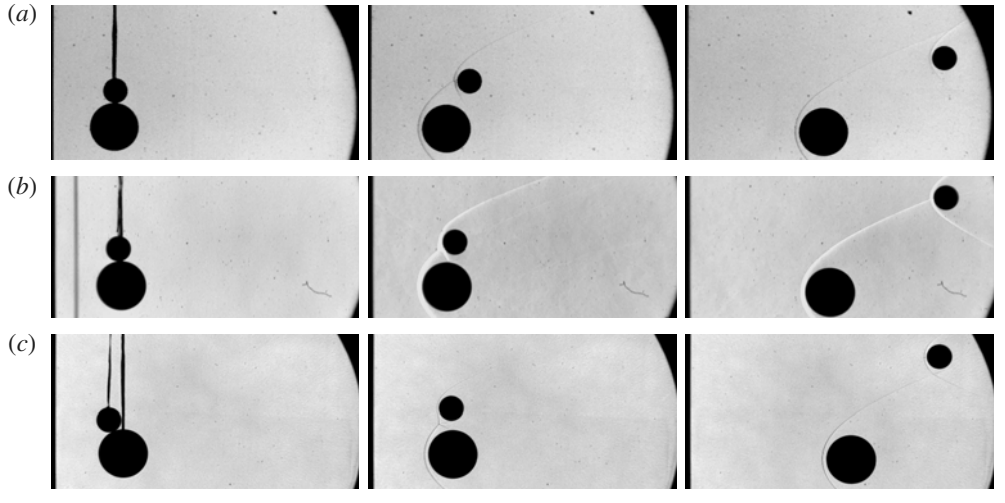

FIGURE 10. Separation behaviour for configurations with a constant radius ratio, $r_2/r_1 = 0.5$, and varying initial alignment angles: (*a*) $\theta_0 = -1.9°$; (*b*) $\theta_0 = 4.1°$; (*c*) $\theta_0 = 22.8°$.

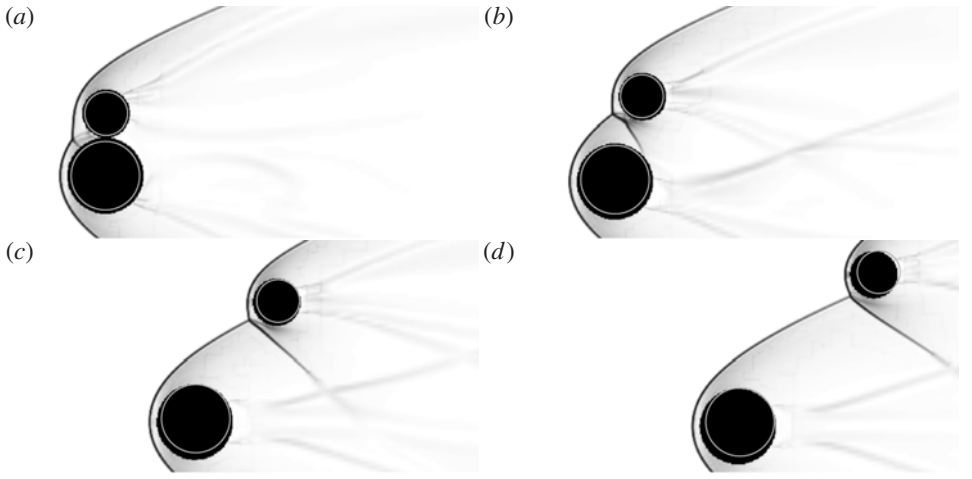

FIGURE 11. Computational schlieren images for $r_2/r_1 = 0.625$, $\theta_0 = -0.7°$, with equivalent experimental sphere positions (corrected for gravity) overlaid; the experimental radii are reduced by 10 % for clarity. Images (*a*), (*b*) and (*d*) correspond to the experimental images of figure 9(*c*).

higher Mach numbers by Laurence & Deiterding (2011). Comparing the trajectories for $r_2/r_1 = 0.5$ and 0.625, it is apparent that the critical radius ratio delineating entrainment from expulsion lies somewhere between these two values.

Now comparing the sequences in figure 10, the effect of varying only the initial alignment angle may be seen, in this case for $r_2/r_1 = 0.5$. Moving the initial secondary position forward relative to the primary sphere (i.e. increasing θ_0) produces a similar effect to increasing the radius ratio, since in either case the secondary body is effectively shifted further outside the primary bow shock. For $\theta_0 = -2°$, the secondary sphere becomes entrained, slightly more quickly than in the $\theta_0 = 0$ case seen in figure 9(*b*). Increasing the alignment angle to 4° results in extended surfing of the secondary body, and it is not clear when the body leaves the visualization window whether it will be ultimately entrained or expelled. Increasing θ_0 further to 23° leads to a trajectory similar to that for $r_2/r_1 = 0.75$, $\theta_0 = -1.1°$ (shown in figure 9*d*), with the secondary body separating rapidly in the lateral direction and soon leaving the influence of the primary shock.

4.2. *Comparison of experimental and computational results*

In this subsection, we compare results from selected experiments and corresponding numerical simulations. In figure 11, computational pseudo-schlieren images are shown for $r_2/r_1 = 0.625$, $\theta_0 = -0.7°$, i.e. the configuration of the verification study of § 3.2. For comparison, equivalent experimental sphere positions have been overlaid, with the sphere radii reduced by 10 % for clarity. The experimental positions have been adjusted to account for the influence of gravity, as is the case for all experimental results presented hereinafter. The non-dimensional time, $t' = \sqrt{\rho_a/\rho_m}tV/r_1$, has been matched between computation and experiment; the respective $t' = 0$ points (i.e. corresponding to $t = T$ in the notation of § 3) were determined in a manner outlined shortly. Images (*a*), (*b*) and (*d*) correspond to the experimental images of figure 9(*c*). A movie comparing the entire separation is included online. Qualitatively, agreement between the sphere trajectories is good, and the experimental shock structures are

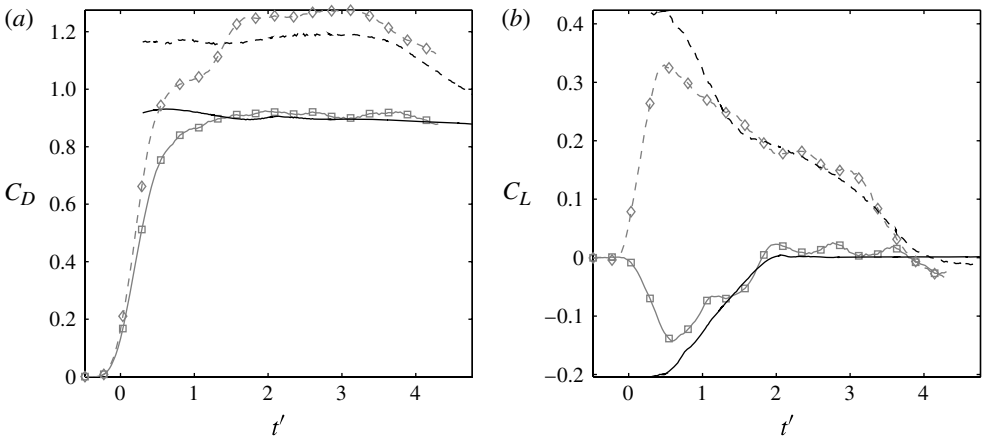

FIGURE 12. Comparison of experimental and computational force coefficients for $r_2/r_1 = 0.5$ and $\theta_0 = -0.1°$: —□—, experimental primary sphere; —, computational primary sphere; −−◇−−, experimental secondary sphere; − − −, computational secondary sphere. The normalized variables are $t' = \sqrt{\rho_a/\rho_m}tV/r_1$, $C_D = 8\rho_m a_x r/(3\rho_a V^2)$ and $C_L = 8\rho_m a_y r/(3\rho_a V^2)$.

accurately reproduced by the computation. However, there is some quantitative disagreement in the sphere positions. The first discrepancy appears in the lateral position of the primary sphere, with the experimental body separating to a lesser degree. The relative trajectories of the secondary spheres are subsequently affected: the experimental sphere is pushed further outwards laterally and also accelerates more rapidly in the axial direction (these effects can be attributed to the increased lift and drag coefficients experienced by a secondary sphere as its position is moved inwards from the free stream towards the primary bow shock – see Laurence & Deiterding 2011). The most likely explanation for the initial discrepancy in the primary sphere motion is the lateral impulse imparted by the detaching threads, as discussed in § 2.5.

In figure 12, we compare force coefficients for $r_2/r_1 = 0.5$, $\theta_0 = -0.1°$ (i.e. the experiment shown in figure 9*b*). Comparisons of additional non-dimensional quantities for this configuration can be found in the online supplementary material. In the numerical simulation, the instant at which the spheres are released is precisely specified; in the experiment, however, the corresponding release instant is not well-defined due to the finite duration of the flow start-up. As the measured velocities provide the clearest indication of the initiation of the sphere motion, the experimental $t' = 0$ point is chosen such that the initial axial velocity profiles of the primary sphere match as closely as possible. After the flow start-up period ($t' \geqslant 1.5$), the numerical simulation underestimates the primary drag coefficient by approximately 1.5 %, which can be attributed to the lack of viscous contributions in the computation. We do not expect to obtain agreement in the force coefficients during the start-up period, as the flow conditions have not yet reached the steady values assumed in the derivation of the experimental coefficients. The secondary drag profiles exhibit larger discrepancies than the primary profiles, the computational curve lying approximately 6 % lower from $t' = 1.5$ to 3.5. This is not surprising, however, considering that the secondary force coefficients will be much more sensitive to the exact relative positions of the spheres, especially in the later stages of the separation when the primary sphere is outside the domain of influence of the secondary sphere. The lift profiles of the primary sphere

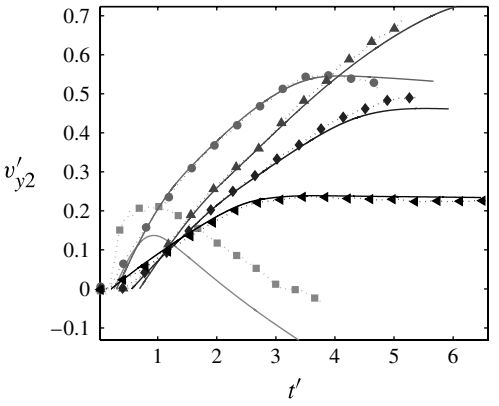

FIGURE 13. Normalized secondary lateral velocity as a function of the non-dimensional time in experiments (symbols) and numerical simulations (lines in matching shades): □, $r_2/r_1 = 0.25$; ○, $r_2/r_1 = 0.5$; △, $r_2/r_1 = 0.625$; ◇, $r_2/r_1 = 0.75$; ◁, $r_2/r_1 = 1$.

also show some discrepancy: this appears to result primarily from a deficit in the repulsive force experienced during the flow start-up, again consistent with the impulse imparted by the threads during detachment. The secondary lift curves show good overall agreement.

As the secondary lateral velocity is the quantity of principal interest here, in figure 13 we compare time-resolved non-dimensional lateral velocities from experiments and numerical simulations for the five configurations shown in figure 9. Agreement for the smallest radius ratio, $r_2/r_1 = 0.25$, is poor. This is because of the low mass of the secondary sphere (0.15 g), which gives rise to both a significant discrepancy in the effective initial alignment angle and a large impulsive velocity imparted by the detaching threads, as discussed in § 2.5. Agreement for $r_2/r_1 = 0.5$ and 1 is very satisfactory, both in the time development of the velocity profiles and in the maximum velocities attained. Slightly larger discrepancies are observed for $r_2/r_1 = 0.625$ and 0.75: although each shows good agreement initially, in the later stages of motion the computational lateral velocity decreases more rapidly than in the experiment, indicating that the computational secondary sphere is being expelled earlier from the flow region bounded by the primary bow shock. The origin of this discrepancy for $r_2/r_1 = 0.625$ has already been discussed in association with figure 11, and the observations made there also apply to $r_2/r_1 = 0.75$. Nevertheless, agreement for these two cases can be considered adequate.

We note that for $r_2/r_1 = 0.25$ and 0.5, the lateral acceleration becomes negative once the secondary sphere is fully entrained within the region bounded by the primary bow shock, indicating that the lateral force is attractive here. This was predicted theoretically by Laurence *et al.* (2007) and is due to the decreasing Pitot pressure moving inwards from the bow shock towards the axis of symmetry of the primary sphere. Thus, the lateral velocity of an entrained secondary sphere reaches a well-defined maximum.

Summarizing these results, with the exception of the $r_2/r_1 = 0.25$ case, the overall agreement observed between experiment and computations is satisfactory. In particular, we conclude that neither the flow start-up period in the experiments nor the lack of physical viscosity in the numerical simulations are significant obstacles to obtaining meaningful quantitative results in the present investigation.

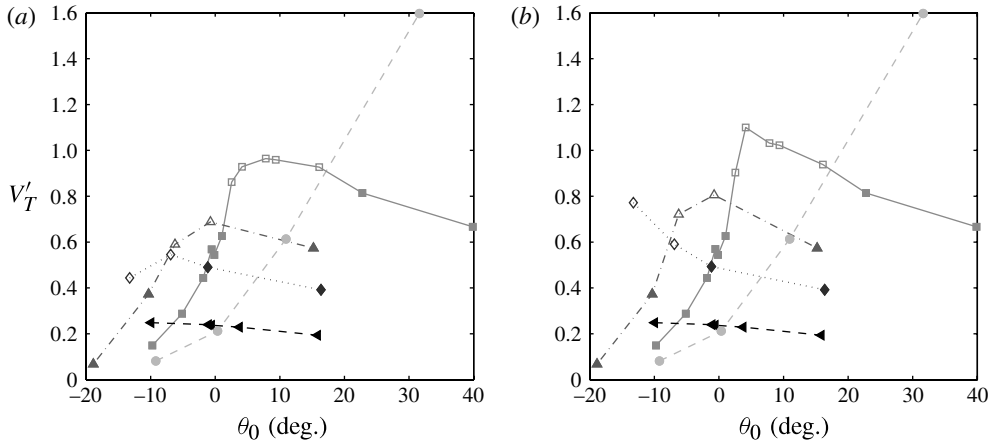

FIGURE 14. Normalized experimental separation velocity of the secondary body as a function of the initial alignment angle with the primary body: ○, $r_2/r_1 = 0.25$; □, $r_2/r_1 = 0.5$; △, $r_2/r_1 = 0.625$; ◇, $r_2/r_1 = 0.75$; ◁, $r_2/r_1 = 1$. Open symbols indicate that the secondary body was still being influenced by the primary shock when it left the visualization area: in (*a*) these points are the directly measured values, whereas in (*b*) the velocities have been extrapolated.

4.3. *Parameterized separation velocities*

We now consider the quantitative variation in the secondary separation velocity as a function of the two independent parameters, θ_0 and r_2/r_1. In figure 14, the normalized separation velocity, V'_T, is plotted versus the initial alignment angle for five radius ratios: $r_2/r_1 = 0.25$, 0.5, 0.625, 0.75 and 1. V'_T, is defined here as the maximum value of v'_{y2} attained during the trajectory. In figure 14(*a*) are plotted directly measured values: solid symbols indicate cases in which the secondary sphere was either entrained or completely expelled within the visualized trajectory; open symbols indicate that the secondary sphere was still being repulsed when it left the visualization window. In order to estimate the final velocity that would result in these latter cases, the lateral acceleration curves were linearly extrapolated based on the final 3.5 ms of visualized flight. The final separation velocities were then taken as the values when these extrapolated accelerations became zero; these results are shown in figure 14(*b*).

For $r_2/r_1 = 1$, V'_T shows only a weak dependence on the alignment angle, increasing from 0.19 for $\theta_0 = 15.8°$ to 0.25 for $\theta_0 = -9.9°$. In all of these experiments, the trajectories of the two spheres took them completely outside the influence of one another's bow shock. For $r_2/r_1 = 0.75$, a stronger effect of the alignment angle is observed, with V'_T increasing more markedly with decreasing θ_0. Again, however, no secondary entrainment was obtained over the range of initial angles considered (-13.2–$16.4°$), indicating that the critical alignment angle delineating entrainment from expulsion for this radius ratio is less than $-13°$. For $r_2/r_1 = 0.625$ and 0.5, a well-defined maximum in V'_T is clearly reached within the range of θ_0 considered: for $r_2/r_1 = 0.5$ this occurs at approximately $\theta_0 = 4.1°$, and for $r_2/r_1 = 0.625$ somewhere between $-6.2°$ and $-0.7°$. As θ_0 is decreased from this critical value, a transition to entrainment occurs and V'_T drops monotonically. For $r_2/r_1 = 0.25$, the secondary sphere was entrained for the three smaller alignment angles and barely expelled at

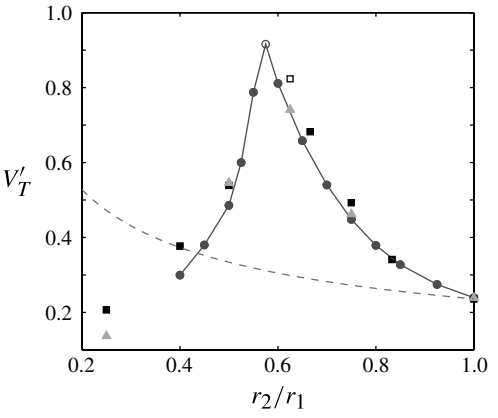

FIGURE 15. Normalized secondary separation velocity versus the radius ratio for initial axial alignment of the sphere centres: □, experimental results; △, refined computational result with identical initial alignment angles to experiments; ○, coarse computational result with $\theta_0 = 0$; – – –, prediction of Passey & Melosh (1980). Open points indicate extrapolated values.

the maximum angle considered (31.6°), indicating that the critical angle lies slightly below this value. The peak separation velocity attained over all alignment angles is seen to increase with decreasing radius ratio, which can be explained by the higher acceleration experienced by a body of smaller mass, all other things being equal.

In figure 15, the normalized separation velocity is plotted as a function of the radius ratio for axially aligned initial configurations (here $|\theta_0| < 1.5°$); for $r_2/r_1 = 0.625$ the extrapolated velocity is used. In addition to the experimental values, we show numerical results from both the refined computations discussed in § 4.2, in which the same alignment angles as in the experiments were specified, and more extensive coarse simulations in which the alignment angle was set uniformly to $\theta_0 = 0$. For the latter, only a single level of grid refinement of factor 3 was employed, and the density ratio, ρ_m/ρ_a, had half the value of the more refined computations. As was noted of the qualitative secondary behaviour in § 4.1, the effect of increasing the radius ratio on V'_T is similar to that of making the alignment angle more positive. As we increase r_2/r_1 from 0.25, V'_T rises sharply until a maximum is reached at the critical ratio, predicted by the coarse simulations to lie at approximately 0.58; thereafter, V'_T drops away steeply to a value of 0.24 for $r_2/r_1 = 1$. This general behaviour is again similar to that observed at higher Mach numbers by Laurence & Deiterding (2011). Comparing the experimental separation velocities with those from the refined numerical simulations, the results are as would be expected from an examination of figure 13. For the smallest radius ratio, $r_2/r_1 = 0.25$, the experimental value is significantly higher because of the low mass of the experimental secondary sphere; an identical secondary sphere was employed for the $r_2/r_1 = 0.4$ experiment, and a similar discrepancy with the coarse numerical result is observed. For $r_2/r_1 = 0.5$ and 1, the experimental and refined numerical results lie very close to one another (with differences of 1.3 % and 1.1 %), but the discrepancies at radius ratios of 0.75 and 0.625 are somewhat larger, at 6 % and 11 %, respectively (though in the latter case, the extrapolation of the experimental result may have exaggerated this difference somewhat). A likely explanation for these differences has been discussed in reference to figure 13. Also shown in figure 15 is the scaling law of Passey & Melosh (1980),

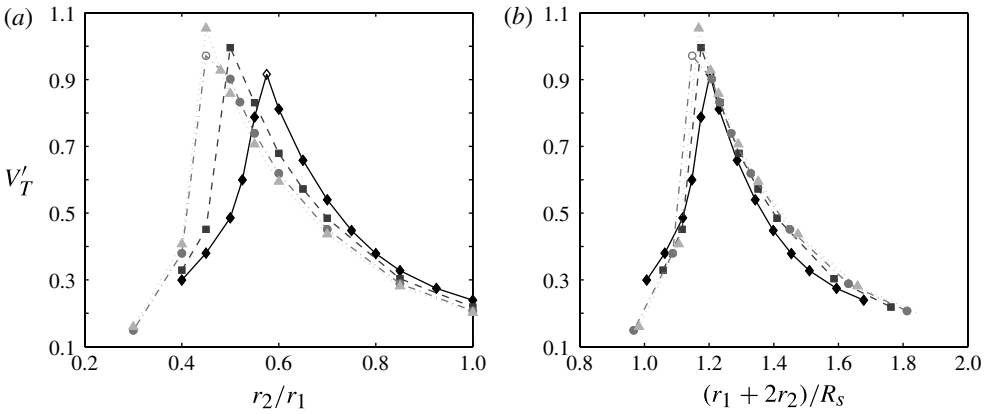

FIGURE 16. Computed normalized separation velocity of the secondary body for different Mach numbers, assuming initial axial alignment of the sphere centres ($\theta_0 = 0$): $\diamond$, $M = 4$; $\square$, $M = 6$; $\bigcirc$, $M = 10$; $\triangle$, $M = 25$. In (*a*), the velocity data are plotted against the radius ratio; in (*b*), the abscissa is the initial lateral location of the outside edge of the secondary sphere normalized by the lateral primary bow-shock displacement at the relevant Mach number.

as given by (1.1). Poor agreement with the experimental and numerical results is observed.

4.4. *Effect of Mach number*

It is clear from comparing the results in figure 15 to those in figure 18 of Laurence & Deiterding (2011) that the separation behaviour is qualitatively similar over the range of Mach numbers considered in the two works ($M = 4$, 10 and 25). It is thus of interest to consider what quantitative differences might exist between the supersonic Mach number considered here and the hypersonic Mach numbers of the earlier study. In figure 16(*a*) we show normalized separation velocities versus the radius ratio for four Mach numbers, all with $\theta_0 = 0$: results for $M = 10$ and 25 are taken from Laurence & Deiterding (2011), the coarse-grid $M = 4$ results from figure 15 are again shown, and an intermediate Mach number of 6 is also included. With the exception of the Mach number, all significant parameters in these computations (e.g. grid resolution, density ratio) were identical, allowing the Mach-number effects to be isolated.

Each of the profiles shows the distinctive peak in separation velocity at the critical radius ratio, with a rapid falling off to either side. It should be noted that the $M = 4$ peak is extrapolated; for the $M = 10$ peak, the lateral acceleration was still increasing when the secondary sphere left the computational domain, and thus a linearly extrapolated velocity could not be calculated. The value of the critical ratio varies between the different Mach numbers, increasing from approximately 0.45 for $M = 25$ to 0.58 for $M = 4$. This variation can be at least partially explained by the growing lateral displacement of the primary bow shock with decreasing Mach number: for a larger shock radius, the secondary sphere will effectively lie further inside the shock at the same initial position, hence a larger radius ratio will be required to achieve the same degree of repulsion. Therefore, in an attempt to scale out the effect of the primary bow-shock location, in figure 16(*b*) we present the same velocity data, but with the abscissa now the scaled distance $(r_1 + 2r_2)/R_s$, where R_s is the radial location of the primary bow shock (at the initial axial location of the

sphere centres) as given by the correlation of Billig (1967). This modified abscissa is thus the initial lateral location of the outer secondary-sphere edge, normalized by the bow-shock displacement. With this choice of scaling the curves collapse much more closely upon one another, indicating that the Mach-number effect observed in figure 16(*a*) is indeed caused primarily by differences in the effective initial position of the secondary sphere relative to the primary bow shock. This collapsing also suggests that the dominant physical phenomena are qualitatively similar over the range of Mach numbers considered.

5. Conclusions

We have carried out an extensive experimental investigation of the dynamical separation characteristics of two initially contiguous spherical bodies in supersonic flow ($M = 4$). In general, the behaviour was found to be similar to that observed analytically and computationally at hypersonic Mach numbers (Laurence & Deiterding 2011). For small radius ratios, the secondary sphere is likely to be entrained within the flow region bounded by the primary bow shock, whereas larger secondary spheres show an increased tendency to be expelled from this region. The likelihood of entrainment increases as the initial position of the secondary sphere is moved downstream relative to the primary sphere. At a critical alignment angle for a given radius ratio (or a critical radius ratio for a given alignment angle), the secondary sphere 'surfs' the primary bow shock, tracing a trajectory so as to follow the shock downstream. This critical angle or radius ratio effectively delineates entrainment from expulsion and also results in the maximum separation velocity with respect to the varied parameter. For $r_2/r_1 = 0.5$, a critical initial alignment angle of approximately 4° was found (with the secondary sphere centre lying upstream of the primary sphere centre); this critical angle varied markedly with the radius ratio, increasing from less than $-13°$ for $r_2/r_1 = 0.75$ to approximately 30° for $r_2/r_1 = 0.25$. For initial axial alignment of the sphere centres, a critical radius ratio of slightly less than 0.625 was deduced. This critical ratio is larger than that found for hypersonic perfect-gas flows (approximately 0.45 for $M \geqslant 10$), a difference that was attributed primarily to the increased lateral displacement of the primary bow shock at lower Mach numbers.

A visualization-based tracking technique allowed quantitative comparisons between the experimental results and high-resolution inviscid numerical simulations. Generally favourable agreement was obtained, the main exception being for a low-mass (<1 g) secondary body, in which case the start-up processes in the experimental facility played a decisive role. Excluding this case, the final separation velocities of the computational and experimental secondary spheres showed agreement to between 1 % and 11 %. This lends a high degree of confidence to both the experimental and computational approaches employed here.

Acknowledgements

The authors wish to thank J. E. Shepherd, whose financial support made the experiments possible, and H. G. Hornung, with whom we had useful discussions.

Supplementary data/movie

Supplementary data/movies are available at http://dx.doi.org/10.1017/jfm.2012.453.

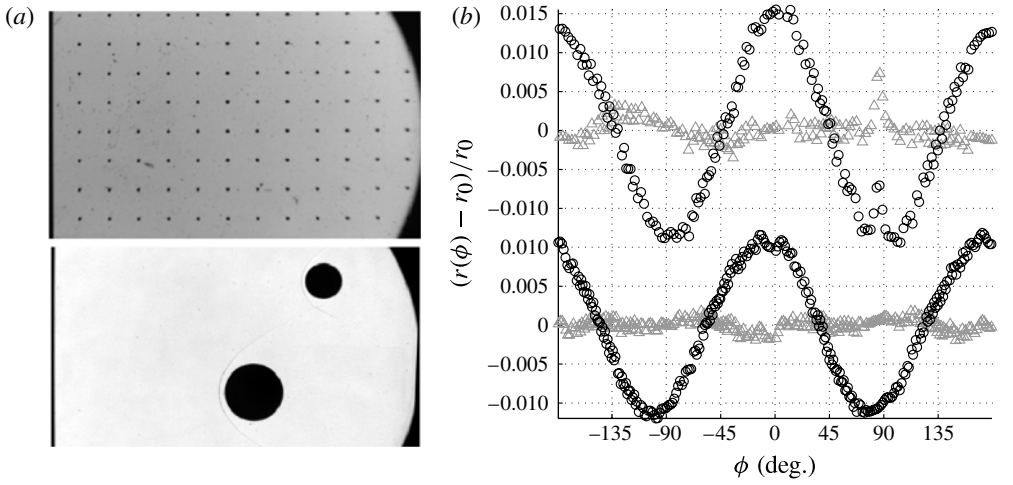

FIGURE 17. (*a*) Images showing the transparent grid used to derive the correction polynomials for optical distortions, and the sphere configuration for which the distortion error is quantified in the accompanying plot. (*b*) Distortion errors in the measured sphere edge points for the primary body (lower profiles) and secondary body (upper profiles): ○, uncorrected points; △, points with distortion correction applied. The anomaly in the corrected secondary profile at 90° is caused by the protrusion due to the remnant of the suspension thread.

Appendix. Correction of distortion errors

In visualization-based measurement techniques, the distortion error associated with the optical set-up can often be problematic. With regard to the technique employed in the present work, optical distortions were noted by Laurence & Karl (2010), but their effect on the tracking technique could not be quantified beyond a rough estimate. Here, with the relatively large range of motion experienced by the spheres, such distortions were found to become a significant factor, and an attempt was made to both characterize and correct for the resulting errors. A transparent plate with circular dimples precision-machined at 25.4 mm intervals was placed inside the test section, and images were recorded with the optical set-up employed for the sphere experiments. The visualized positions of the dimples were determined using the tracking routine described in § 2.4 and compared to a uniform grid. A third-order polynomial transformation between image coordinates, $(\hat{x}, \hat{y})$, and physical coordinates, (x, y), was then defined for each of x and y, e.g. $x = a + b\hat{x} + c\hat{y} + d\hat{x}^2 + e\hat{x}\hat{y} + f\hat{y}^2 + g\hat{x}^3 + h\hat{x}^2\hat{y} + i\hat{x}\hat{y}^2 + j\hat{y}^3$, and the coefficients were determined by a least-squares fit over all determined dimple positions.

With the coefficients for each of x and y thus calculated, the correction was incorporated into the tracking algorithm by applying it to the detected edge points prior to the fitting of the circular profiles. Applying the transformation directly to the image would also be possible, but would be more expensive computationally. A typical reduction in the distortion of the sphere profiles enabled by this correction is shown in figure 17. The deviation between the radii of the detected edge points and the overall fitted radius is plotted here against the internal angle, ϕ, for each of the two spheres in the image shown (normalized by the fitted radius in each case), for both the original and corrected edge points. The deviation for the larger sphere, which originally reaches 1 %, is reduced by a factor of approximately 10, while the

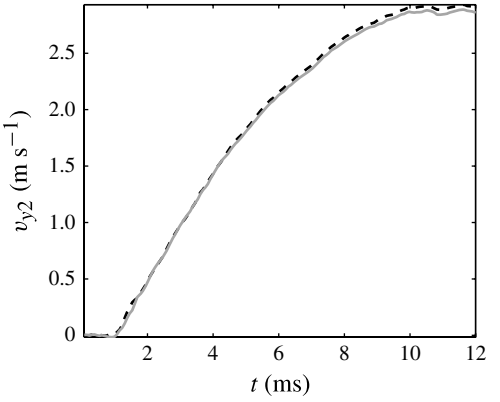

FIGURE 18. Example of the effect of the distortions present in the optical system on the measured lateral velocity of the secondary body: – – –, corrected; —, uncorrected.

reduction for the smaller sphere is by a factor of 6. Furthermore, the root-mean-square (r.m.s.) deviation in both cases is now approximately 0.03 pixels, which is close to the expected accuracy of the edge detection routine under noisy conditions (Laurence & Karl 2010); or 10 μm, which is near the quoted sphericity of the spheres employed (13 μm).

As the quantity of main interest in the present study is the lateral separation velocity of the secondary body, in figure 18 is plotted an example of a time-resolved lateral velocity profile, both with and without the distortion correction incorporated into the measurements. The discrepancy between the two results is initially negligible, but grows to 1.7 % by the time the maximum lateral velocity is reached. As the correction employed has already reduced the error in the sphere profile by a factor of 6, we can roughly estimate the remaining velocity error to be of the order of 0.3 %. Given the other experimental uncertainties discussed in § 2.5, any further improvement to the distortion correction is unlikely to offer significant benefits.

REFERENCES

ARTEM'EVA, N. A. & SHUVALOV, V. V. 1996 Interaction of shock waves during the passage of a disrupted meteoroid through the atmosphere. *Shock Waves* **5**, 359–367.

ARTEMIEVA, N. A. & SHUVALOV, V. V. 2001 Motion of a fragmented meteoroid through the planetary atmosphere. *J. Geophys. Res.* **106** (E2), 3297–3309.

BERGER, M. & COLELLA, P. 1988 Local adaptive mesh refinement for shock hydrodynamics. *J. Comput. Phys.* **82**, 64–84.

BILLIG, F. S. 1967 Shock-wave shapes around spherical- and cylindrical-nosed bodies. *J. Spacecr. Rockets* **4** (6), 822–823.

BOROVIČKA, J. & KALENDA, P. 2003 The Morávka meteorite fall: 4 Meteoroid dynamics and fragmentation in the atmosphere. *Meteorit. Planet. Sci.* **38** (7), 1023–1043.

CANNY, J. 1986 A computational approach to edge detection. *IEEE Trans. Pattern Anal. Mach. Intell.* **8** (6), 679–698.

DEITERDING, R. 2003 Parallel adaptive simulation of multi-dimensional detonation structures. PhD thesis, Brandenburgische Technische Universität Cottbus.

DEITERDING, R. 2005*a* Construction and application of an AMR algorithm for distributed memory computers. In *Adaptive Mesh Refinement – Theory and Applications* (ed. T. Plewa, T. Linde & V. G. Weirs). *Lecture Notes in Computational Science and Engineering,* vol. 41, pp. 361–372.

DEITERDING, R. 2005*b* Detonation structure simulation with AMROC. In *High Performance Computing and Communications 2005* (ed. J. Dongarra, L. T. Yang, O. F. Rana & B. Di Martino). *Lecture Notes in Computer Science,* vol. 3726, pp. 916–927.

DEITERDING, R. 2009 A parallel adaptive method for simulating shock-induced combustion with detailed chemical kinetics in complex domains. *Comput. Struct.* **87**, 769–783.

DEITERDING, R. 2011*a* Block-structured adaptive mesh refinement – theory, implementation and application. *ESAIM Proc.* **34**, 97–150.

DEITERDING, R. 2011*b* High-resolution numerical simulation and analysis of Mach reflection structures in detonation waves in low-pressure $H_2 : O_2 :$ Ar mixtures: a summary of results obtained with the adaptive mesh refinement framework AMROC. *J. Combust.* **2011**, Article ID 738969, 18 pages.

DEITERDING, R., CIRAK, F., MAUCH, S. P. & MEIRON, D. I. 2007 A virtual test facility for simulating detonation- and shock-induced deformation and fracture of thin flexible shells. *Intl J. Multiscale Comput. Engng* **5** (1), 47–63.

DEITERDING, R., RADOVITZKY, R., MAUCH, S. P., NOELS, L., CUMMINGS, J. C. & MEIRON, D. I. 2005 A virtual test facility for the efficient simulation of solid materials under high energy shock-wave loading. *Engng Comput.* **22** (3–4), 325–347.

FEDKIW, R. P., ASLAM, T., MERRIMAN, B. & OSHER, S. 1999 A non-oscillatory Eulerian approach to interfaces in multimaterial flows (the ghost fluid method). *J. Comput. Phys.* **152**, 457–492.

HOERNER, S. F. 1965 *Fluid-Dynamic Drag: Practical Information on Aerodynamic Drag and Hydrodynamic Resistance*. Hoerner Fluid Dynamics.

LAURENCE, S. J. 2012 On the tracking of rigid bodies through edge-detection and least-squares fitting. *Exp. Fluids* **52** (2), 387–401.

LAURENCE, S. J. & DEITERDING, R. 2011 Shock-wave surfing. *J. Fluid Mech.* **676**, 396–431.

LAURENCE, S. J., DEITERDING, R. & HORNUNG, H. G. 2007 Proximal bodies in hypersonic flow. *J. Fluid Mech.* **590**, 209–237.

LAURENCE, S. J. & KARL, S. 2010 An improved visualization-based force-measurement technique for short-duration hypersonic facilities. *Exp. Fluids* **48** (6), 949–965.

MOFFAT, R. J. 1982 Contributions to the theory of single-sample uncertainity analysis. *Trans. ASME: J. Fluids Engng* **104** (2), 250–260.

MOUTON, C. A. & HORNUNG, H. G. 2008 Experiments on the mechanism of inducing transition between regular and Mach reflection. *Phys. Fluids* **20**, 126103.

PASSEY, Q. R. & MELOSH, H. J. 1980 Effects of atmospheric breakup on crater field formation. *Icarus* **42**, 211–233.

SETTLES, G. S. 2006 *Schlieren and Shadowgraph Techniques*. Springer.

ZIEGLER, J. L., DEITERDING, R., SHEPHERD, J. E. & PULLIN, D. I. 2011 An adaptive high-order hybrid scheme for compressive, viscous flows with detailed chemistry. *J. Comput. Phys.* **230** (20), 7598–7630.